Force Sensing Shell using a Planar Sensor for Miniature Legged Robots

Joshua D. Goldberg
Ronald S. Fearing

Electrical Engineering and Computer Sciences
University of California at Berkeley

May 1, 2016

Force Sensing Shell using a Planar Sensor for Miniature Legged Robots

by Joshua D. Goldberg

Research Project

Submitted to the Department of Electrical Engineering and Computer Sciences, University of California at Berkeley, in partial satisfaction of the requirements for the degree of **Master of Science, Plan II**.

Approval for the Report and Comprehensive Examination:

Committee:

Prof. Ronald S. Fearing

Research Advisor

Date

* * * * * *

Prof. Ruzena Bajcsy

Second Reader

Date

Abstract

Mobile robot contact sensing can be useful for navigation and manipulation with small robots. In this work, we present a low-cost, 40 gram force-torque sensor for a 10 cm hexapedal millirobot. A planar array of photointerrupters, rigidly attached to the structure of the robot, is used to measure the six-axis movement of a shell attached to the robot with springs. The sensors measure the intensity of infrared light reflected off of a surface on the underside of the shell, which has been specially designed to enable the resolution of the forces and moments in the x-, y-, and z-axes applied to the shell. The sensor has a force sensitivity of 17 mN and torque sensitivity of 0.72 mN-m for a sampling rate of 100 Hz. The sensor can resolve a force equivalent to 2.4% of the combined robot and sensor weight of 700 mN.

Contents

List of Figures

List of Tables

Chapter 1

Introduction

Real-world environments are riddled with moisture, dirt, and other small particulates. In order for robots to operate safely in the field, it is necessary for them to be fully enclosed, such that their sensitive electronics are not exposed to these elements. However, protective layers typically occlude sensors, making it more difficult for the robot to sense its environment. For example, while obstacle detection using computer vision [1][16] or ultrasonic rangefinders [4] are very effective methods that enable robot path planning, they rely on clean, clear camera lenses and emitter-detector pairs, respectively. Even covering these sensors with a transparent shell renders the robot blind if the shell becomes dirty. Thus, an alternative method for sensing obstacles in a robot's vicinity is desired.

One approach is to physically touch and feel objects rather than perceive them visually. Furthermore, making physical contact with surroundings can be sufficient for identifying friendly from impassable terrain. Hair sensor arrays have been used to understand terrain beneath a robot [10]. There have been many efforts in object detection and wall following. Whisker technologies have been developed by Wijaya [20] and Russell [15] as well as instrumented antennae by Lee [12] and Lamperski [11]. To sense tactile forces, Liljeback [13][14] embedded sensors into the joint modules of snake robots to improve locomotion. Commercial six-axis force-torque sensors have also been used between a robot and an encompassing shell, as shown by Tsuji [18].

The Biomimetic Millisystems Lab at U.C. Berkeley is working towards developing low-cost, disposable, bio-inspired millirobots, with masses below 100 grams and lengths

on the order of ten centimeters. Thus, heavy, expensive commercial sensors are infeasible for our application. Due in part to the rising ubiquity of the smartphone, a broad assortment of integrated sensors has become widely available. Accelerometers and gyroscopes can be useful for robotic tactile feedback because they can detect impacts, such as running into a wall or an object falling on a robot; they can also detect if a robot becomes inverted.

However, these sensors cannot measure static loads, and cannot detect, for instance, if the object that fell on the robot continues to trap it, or if it slid off. Thus, a tactile force sensor is required to enable this functionality. Optical proximity sensors have also become cheap and lightweight, and they were used by Hirose [7] to successfully develop a six-axis force-torque sensor. Additionally, Sinden and Boie [17] designed planar capacitive sensors to measure six-axis forces and torques. A planar sensor is of high value, as it can be implemented on a printed circuit board. In this work, a low-cost, lightweight tactile sensor using planar photointerrupters is developed, which is capable of measuring six-axis forces and torques with resolutions on the order of ten millinewtons and five tenths of a millinewton-meter, respectively.

Chapter 2

Methods

Robot Platform and Technology Overview

The robot used in this work is the VelociRoACH (Fig. 2.1), a 30 gram, 10 cm long hexapedal millirobot [6]. It is manufactured using the Smart Composite Microstructures (SCM) process [8], which allows the robot to be folded together from planar parts. The VelociRoACH is one of the fastest running robots relative to scale, and its design was inspired by the American Cockroach because of the insect's variety of stable, high speed gaits [6].

The VelociRoACH has been modified to carry additional hardware for tactile sensing, which is detailed in Fig. 2.2. The main microcontroller printed circuit board, referred to here as the ImageProc, is responsible for controlling the gait of the robot and recording telemetry data. It communicates with the tactile sensing printed circuit board, referred to in this work as the SkinProc, which is based off previous work by Karras [9]. Photointerrupters, which are surface mounted to the SkinProc (Fig. 2.3) measure the intensity of light reflected by reflectors attached to springs above the robot. A polycarbonate shell is rigidly attached to the reflectors, which has been thermoformed to a 3D printed mold [5]. The forces and torques seen by the shell are coupled onto the reflector plate, causing displacement that is measured by the photointerrupters on the SkinProc. From this displacement, the six-axis forces and torques on the VelociRoACH's shell are reconstructed.
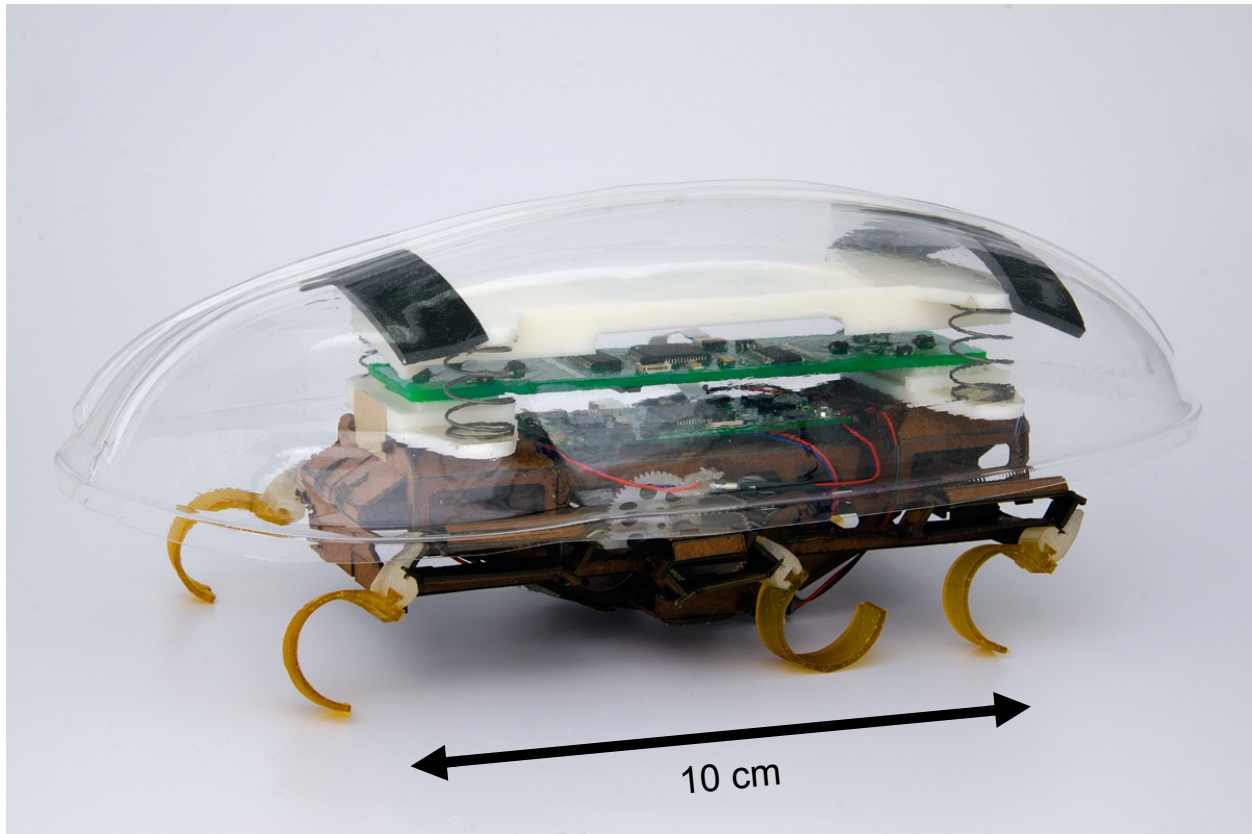
Figure 2.1: Force-torque sensor and shell mounted on a VelociRoACH.

Optical Proximity Sensing

The sensors are commercially available compact photointerrupters (Sharp GP2S60) with a footprint of 5.44 mm^2. The light emitter is a gallium arsenide non-coherent infrared emitting diode with a maximum emitted wavelength of 950 nm. The light detector is a silicon phototransistor with a maximum sensitivity wavelength of 930 nm. The package has been designed such that the diode and phototransistor are oriented in the same direction, there is no light leakage from the emitter to the detector, and visible light is prevented from exciting the detector. As is shown in Fig. 2.3, there are eight sensors on the SkinProc, and eight corresponding reflectors on the reflector plate (the design of which is discussed in the following section). The SkinProc contains two 16-channel multiplexers: the first controls the power supply lines for the emitter-detector pairs and the second controls the detector measurement lines. Thus, it is possible to create an array of
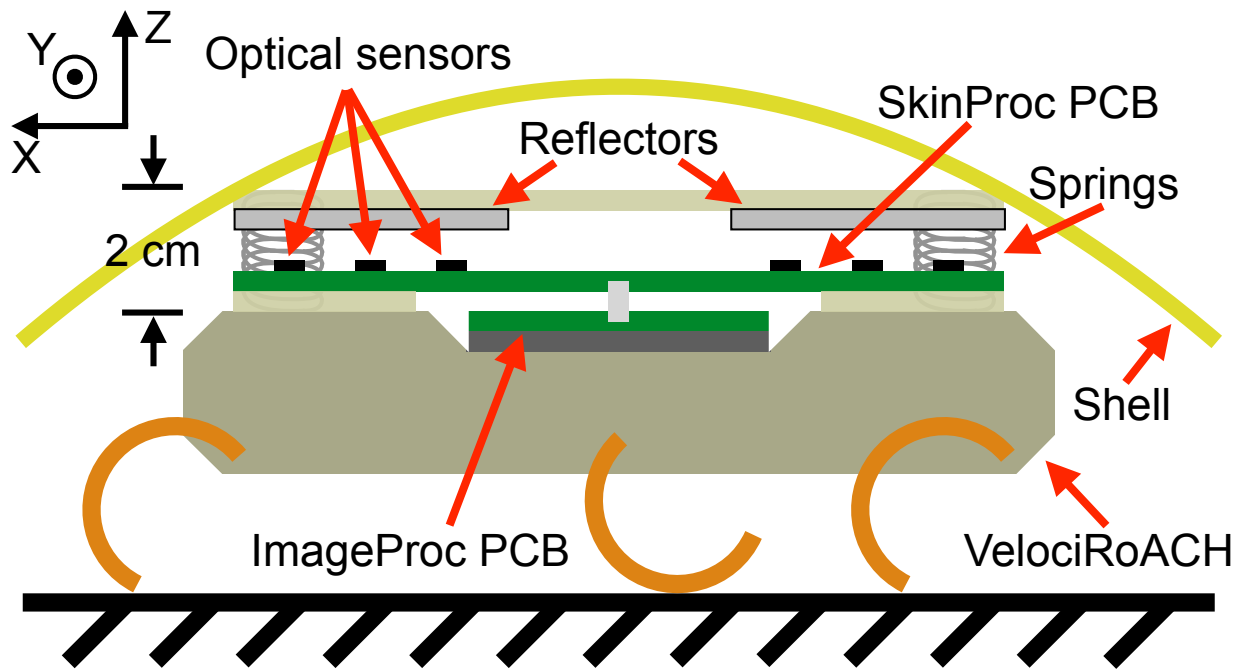
Figure 2.2: Side view of sensor and shell mounted on a VelociRoACH, showing optical proximity sensors and sensing springs.
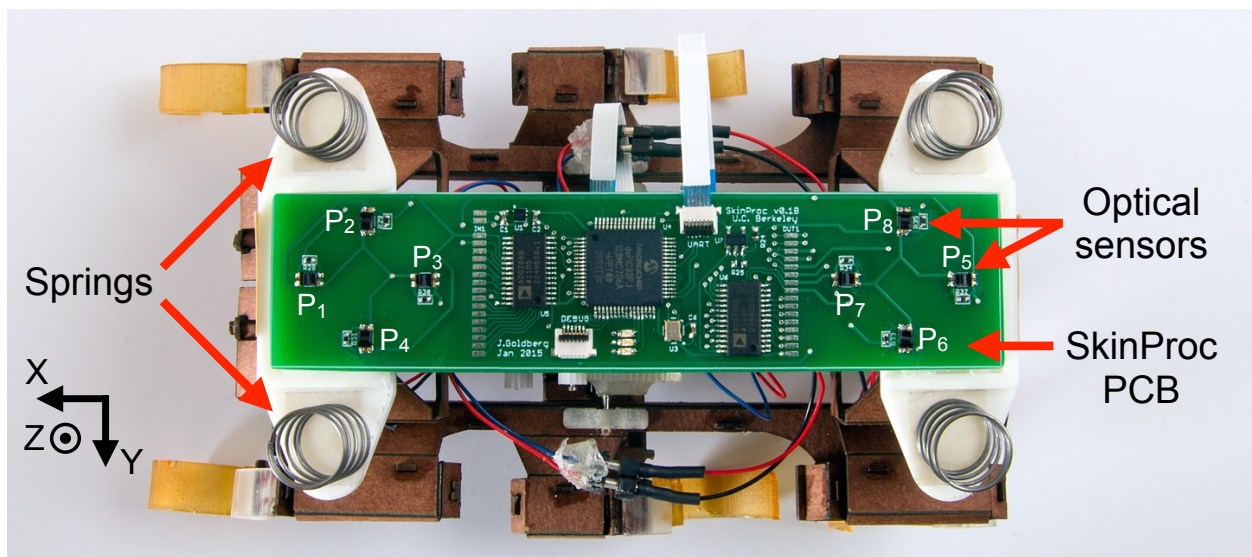
Figure 2.3: Photo showing custom SkinProc sensing board with 8 proximity sensors mounted in two arrays.
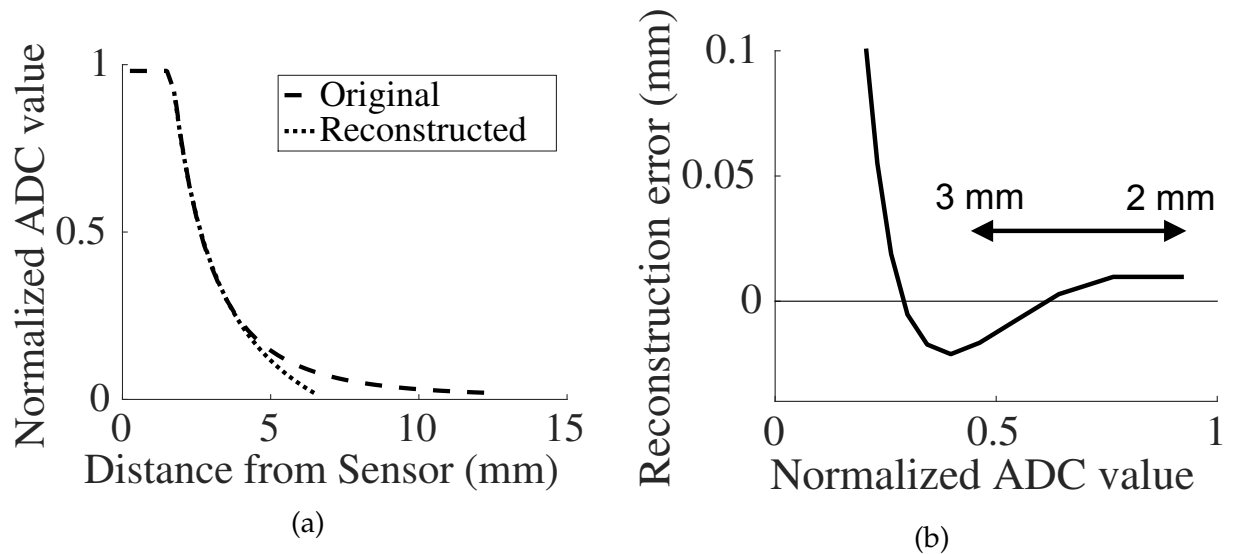
Figure 2.4: Response of individual sensor. (a) Proximity sensor response, and $1/r$ fit to curve. (b) Fitting error over 2-5 mm range, with error over most sensitive 2-3 mm range of less than 20 μm.

up to 16 rows and 16 columns of sensors, and selectively measure only one at a time. For this configuration of eight photointerrupters, only one is powered by each supply line, in order to eliminate the possibility of stray light from an adjacent emitter entering the active detector. The measurement lines feed the current from the phototransistor into a current-to-voltage amplifier, the output of which is read by the 12-bit analog to digital converter of the microprocessor. A full frame of the eight sensor readings is passed to the ImageProc at approximately 100 Hz, which can then be used by the robot to make decisions.

To reconstruct reflector height from sensor output, the least squares method was used to fit a $1/r$ curve to the 2-4 mm range of sensor data. Fig. 2.4a displays the original data as well as the result of the fit. The fit is very good, with $R^2 > 0.999$ and a worst-case error less than 20 μm for the most sensitive 2-3 mm range, as is shown in Fig. 2.4b. The linear least squares problem is formulated in Eqn. (2.1), where s represents the sensor value, r is the range, and a and b are the coefficients that are solved for. Once a and b are found,

Eqn. (2.2) can be used to solve for the reconstructed range $\hat{r}$.

$$s = \begin{bmatrix} \frac{1}{r} & 1 \end{bmatrix} \begin{bmatrix} a \\ b \end{bmatrix} , \tag{2.1}$$

$$\hat{r} = \frac{a}{s - b} , \tag{2.2}$$

This method, when used to calibrate all eight sensors of the SkinProc, enables us to determine the height of each reflector with great accuracy. For static reflector height, there is a standard deviation of only 1 bit in the measurements by the ADC.

Reflector Design

Because each sensor can be calibrated to accurately measure the height of the reflector above it, it is then possible to measure the height of a simple reflective plane parallel to the SkinProc moving up and down in the z-axis. In this case, the sensors will not respond to a horizontal displacement of the reflector along the xy-plane because the reflector will remain the same height through the movement. However, if the reflector plane is rotated about the y-axis, like the reflector on the right in Fig. 2.5a, the height of the point on the reflector directly above the sensor will vary with displacements in both the x-axis as well as the z-axis. The sensor now reacts to two degrees of freedom. This is demonstrated in Fig. 2.6, where a single panel of reflectors can be designed such that one sensor reacts to lateral displacement along an axis, while the other two sensors stay relatively constant. Building upon this, the eight reflectors were designed to cause the sensors to react orthogonally to motion spanning six degrees of freedom, much in the same way Sinden and Boie were able to arrange capacitors that reacted orthogonally to span six degrees of freedom [17].

The product of our design can be seen in Fig. 2.5b, where four reflectors are parallel to the xy-plane such that they react to z-axis displacements, two are rotated about the y-axis such that they react to x- and z-axis displacements, and the remaining two are rotated about the x-axis such that they react to y- and z-axis displacements. Using the lengths between sensors and small angle approximations for rotations, there is a linear mapping
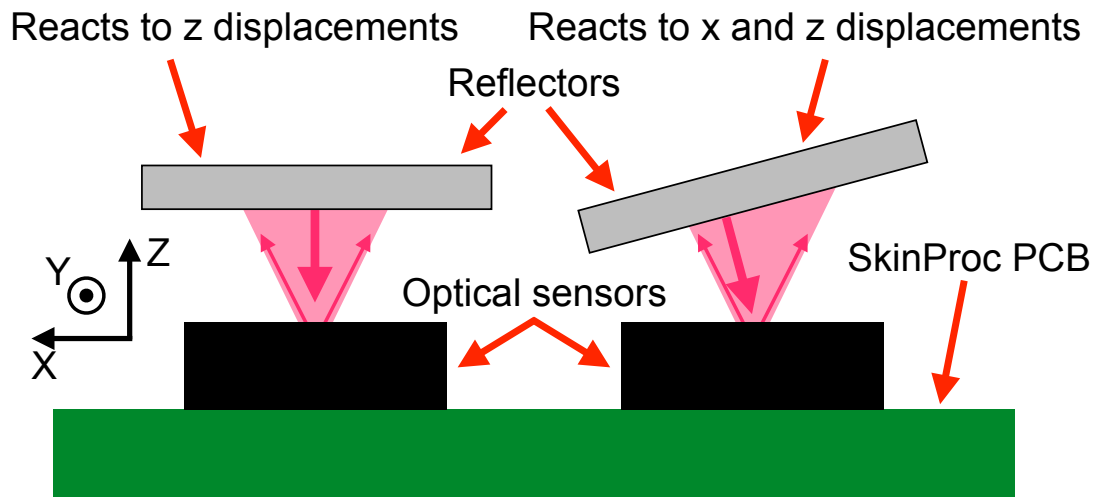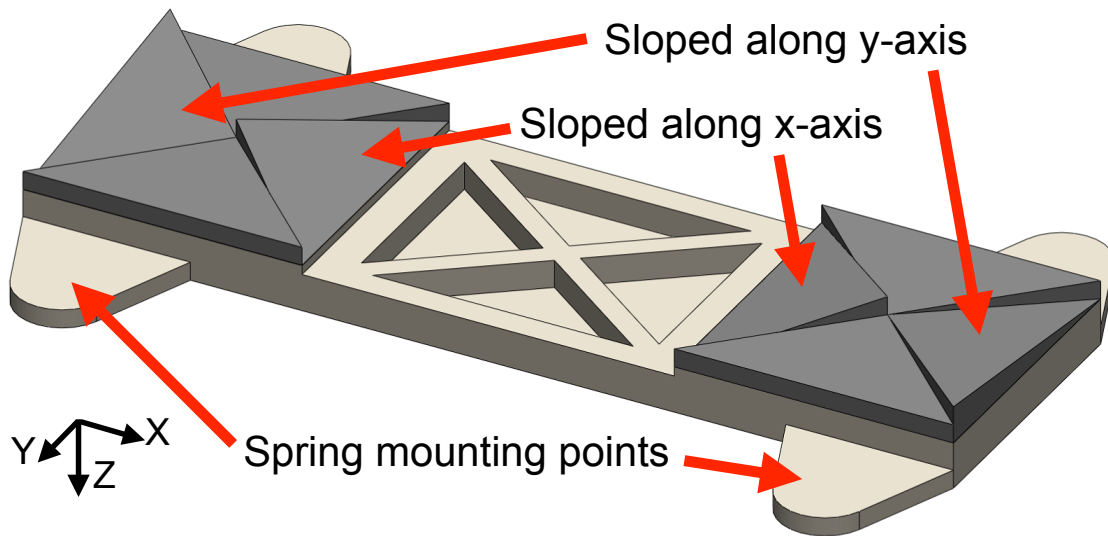
Figure 2.5: Principle of operation of force-torque sensor. (a) Spring supported reflective element has sloped reflector geometry that responds to lateral and normal displacement. (b) Complete floating reflective element with 4 reflectors at each end, corresponding to each of 8 proximity sensors.
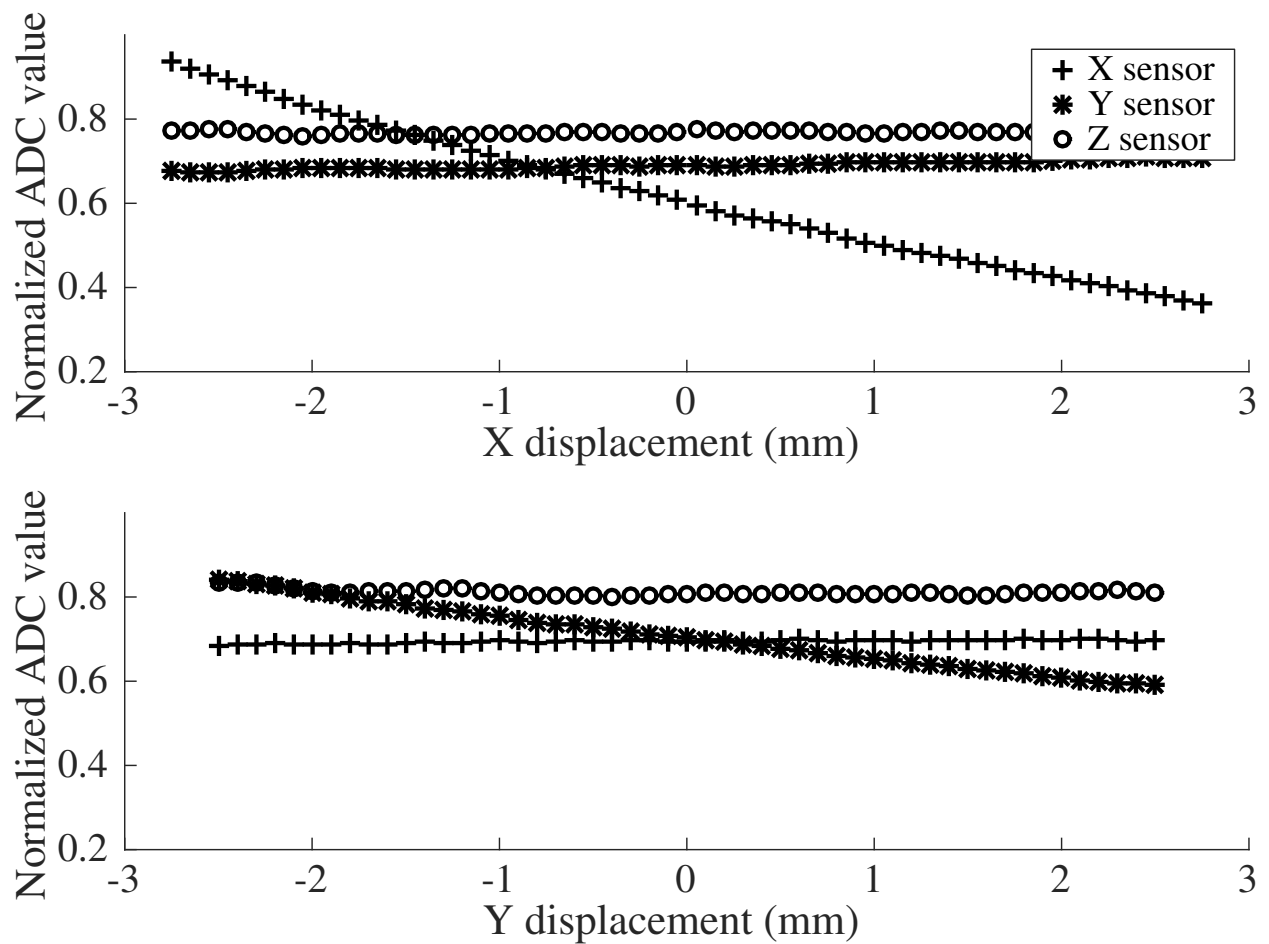
Figure 2.6: Sensor displacement test for three sensing elements. Top plot shows response of sensors to *x* displacement, and bottom plot shows response to *y* displacement, indicating that sensor responses are relatively independent.

between the six spatial degrees of freedom and the height that each of the eight sensors would measure with this reflector design. This is seen in Eqn. (2.3).

$$
\begin{bmatrix} R_1 \\ R_2 \\ R_3 \\ R_4 \\ R_5 \\ R_6 \\ R_7 \\ R_8 \end{bmatrix} = \begin{bmatrix} 0 & c_y & 1 & 0 & -l_{15}/2 & c_y*l_{15}/2 \\ 0 & 0 & 1 & -l_{24}/2 & -l_{28}/2 & 0 \\ c_x & 0 & 1 & 0 & -l_{37}/2 & 0 \\ 0 & 0 & 1 & l_{24}/2 & -l_{46}/2 & 0 \\ 0 & -c_y & 1 & 0 & l_{15}/2 & c_y*l_{15}/2 \\ 0 & 0 & 1 & l_{68}/2 & l_{46}/2 & 0 \\ -c_x & 0 & 1 & 0 & l_{37}/2 & 0 \\ 0 & 0 & 1 & -l_{68}/2 & l_{28}/2 & 0 \end{bmatrix} \begin{bmatrix} x \\ y \\ z \\ \theta_x \\ \theta_y \\ \theta_z \end{bmatrix}, \tag{2.3}
$$

The constants c_x and c_y in Eqn. (2.3) are the slopes of the reflectors reacting to x- and y-axis displacements, respectively. These are necessary to calculate the change in height seen by the sensor for lateral translations. The l_{mn} constants in Eqn. (2.3) are the lengths between sensors; for example l_{15} is the length between sensors P_1 and P_5 (sensor numbers are labeled in Fig. 2.3). The coefficients matrix in Eqn. (2.3) is rank 6, so its pseudoinverse can be calculated in order to left multiply the column vector of reconstructed heights R_{1-8} to reconstruct the six degrees of freedom. This validates the reflector design in Fig. 2.5b, because the rank 6 linear mapping confirms that the reflector geometry allows recovery of all displacements and rotations in the xyz-coordinate system.

Sensor to Force-Torque Calibration

The previous section shows that the sensor can resolve movement in six degrees of freedom, and thus can be used as a six-axis force-torque sensor. While it would be possible to calculate forces and torques directly from the displacements and rotations of the shell, this would involve a rigorous characterization of the springs as they move in six degrees of freedom with the shell. Instead, work done by Bicchi [2][3] as well as Voyles et al. [19] was drawn upon to calibrate the force-torque sensor. While recording sensor data from the SkinProc, a commercial force-torque sensor (ATI Nano43) under the VelociRoACH was used to continuously measure a range of forces and torques manually applied to the shell to sweep through most of the input space (because this was done by hand, the forces and torques applied could not be fully exhaustive). Then a polynomial least squares fit

was solved between the data from the commercial sensor and the data from the SkinProc. Each set of eight sensor values was arranged as in Eqn. (2.4) and Eqn. (2.5), and each set of measured force-torque values was arranged as in Eqn. (2.6).

$$s_1^* = \begin{bmatrix} s_1 & s_1^2 & s_1^3 \end{bmatrix}, \tag{2.4}$$

$$S = \begin{bmatrix} s_1^* & s_2^* & \dots & s_8^* \end{bmatrix}, \tag{2.5}$$

$$M = \begin{bmatrix} F_x & F_y & F_z & M_x & M_y & M_z \end{bmatrix}, \tag{2.6}$$

The least squares equation was formulated with $n = 97526$ samples, as in Eqn. (2.7) and Eqn. (2.8). A pseudoinverse as in Eqn. (2.9) was used to solve for C, the 24x6 calibration matrix that maps sensor data to forces and torques.

$$M = SC, \tag{2.7}$$

$$\begin{bmatrix} M_1 \\ M_2 \\ \vdots \\ M_n \end{bmatrix} = \begin{bmatrix} S_1 \\ S_2 \\ \vdots \\ S_n \end{bmatrix} C = \begin{bmatrix} S_1 \\ S_2 \\ \vdots \\ S_n \end{bmatrix} \begin{bmatrix} c_{1,1} & \dots & c_{1,6} \\ c_{2,1} & \dots & c_{2,6} \\ \vdots & \ddots & \vdots \\ c_{24,1} & \dots & c_{24,6} \end{bmatrix}, \tag{2.8}$$

$$C = (S^T S)^{-1} S^T M, \tag{2.9}$$

Chapter 3

Results

Force-Torque Estimation

The calibration step was performed with $n = 97526$ samples, the calibration data set. To create this calibration data set, forces between about ± 1 N and torques between about ± 60 mN-m were applied manually and slowly to the shell in all axes while the SkinProc proximity sensor values and the forces and torques from the commercial sensor were recorded. This input range was used to prevent the sensor from saturating. This data set was used to generate the sensor response matrix, C in Eqn. (2.9), to be used to map proximity sensor values to forces and torques. Another data set was gathered, the test data set, which was a non-exhaustive set with $n = 42316$ samples. The test data was also created with manually applied forces between about ± 1 N and torques between about ± 60 mN-m. The sensor response matrix was then applied to the proximity sensor values of the test data set to estimate the forces and torques applied to the shell. These estimates are compared to the true values from the commercial sensor in Fig. 3.1. It is apparent that there are a few instances in which the reconstruction produces some error, but in general, the estimated forces and torques follow the true data relatively closely for each of the six axes.

Another indicative way to visualize the success of the sensor response matrix at mapping proximity sensor values to forces and torques is to eliminate the time component of the test data set and directly compare the true data and the estimated data. Fig. 3.2 shows
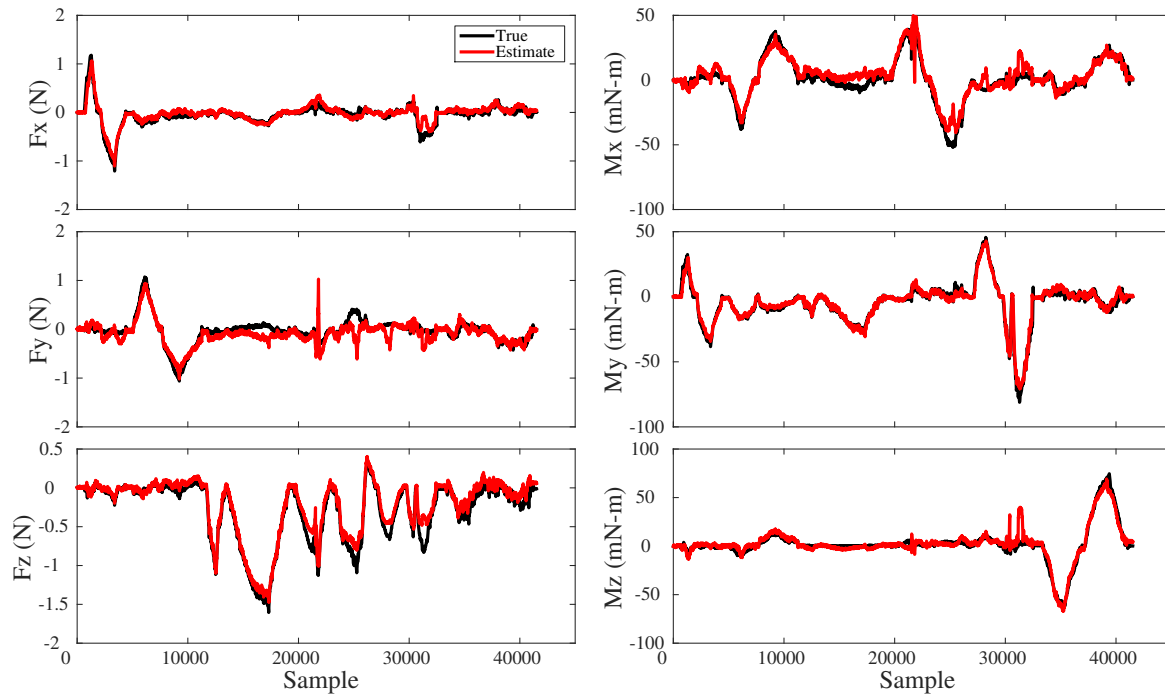
Figure 3.1: Comparison of true and estimated forces and torques for the test data set. True data was recorded using the commercial force-torque sensor and estimated data was calculated by applying the sensor response matrix to the SkinProc proximity sensor data.

the estimated data versus the true data for each of the three forces and three torques. For each force and torque, the majority of the data points fall in a relatively tight band around the dashed line with slope of 1, which indicates an ideal 1-to-1 linear mapping. There are indeed some obvious outliers, which speak to the fact that the sensor is not perfect for all forces and moments applied to the shell. However, it is not expected to be the case that this cheap, lightweight sensor would have the accuracy and precision of an expensive commercial force-torque sensor like the one used in the calibration step. Thus, it is tolerable to have a small degree of error in the force-torque estimates.

Table 3.1 shows the median percent error between true and estimated forces and torques for each axis of the test data set. Because the error distributions become skewed as a result of very large percent errors that arise when the true force is almost zero, these medians are calculated for individual force magnitudes above 0.2 N and torque magnitudes above 10 mN-m (a 0.2 N force applied 5 cm away from the axis of rotation). Table
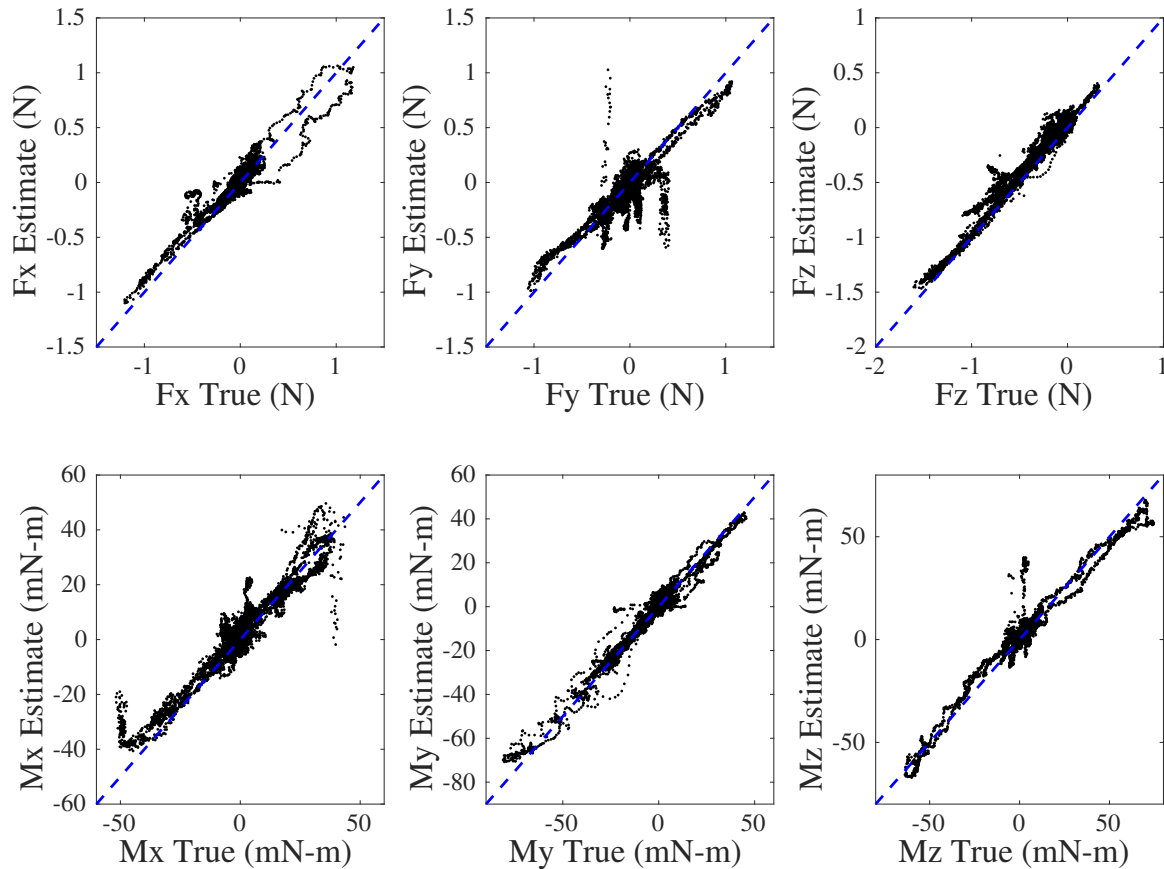
Figure 3.2: Measured and reconstructed force-torque data compared directly. Time is eliminated in order to visualize the linearity of the mapping over a range of forces and torques. The dashed lines have slopes of 1, indicating an ideal 1-to-1 linear mapping.

3.1 also shows the worst case error for each axis as a percentage of the maximum range applied to the given axis in the test data set.

The fit method previously discussed has only been verified for the experiments detailed in the following sections. There is also a small constant offset for certain axes, thus an average is used to zero the measurements.

Gravity Vectors

To further analyze the performance of the system, the force vector measured by the Skin-Proc was compared to the acceleration vector measured by the accelerometer on the ImageProc. Theoretically, these two vectors should be aligned parallel with gravity when no

Table 3.1: Median percent error and worst case error as a percentage of range for the estimated forces and torques for the test data set (n=42316).

	F_x	F_y	F_z	M_x	M_y	M_z
Median percent error	18%	18%	16%	15%	7.6%	11%
Worst case error	20%	59%	25%	43%	19%	28%

other acceleration is enacted on the robot. To test this, a 50 gram mass was rigidly attached to the top of the shell of the VelociRoACH and data was collected while the robot was rotated clockwise around its x- and y-axes slowly at a constant velocity to not expose the robot to any acceleration besides gravity. As the robot was rotated first around its y-axis and then around its x-axis, the acceleration traces of both the shell and the accelerometer follow approximately the same paths, as is apparent in Fig. 3.3. The acceleration measured by the shell here was calculated by dividing the reconstructed forces by the 50 gram mass (Solving for a in Newton's second law of motion $F = ma$). Because the calibration step did not take into account extensive data for upward forces on the shell, the system reports about half the correct acceleration when the robot is inverted. This is more apparent in Fig. 3.4, which shows slices of the three-dimensional acceleration vector space. Here, the shell underestimates the force of gravity when it is inverted, which is illustrated by the Az component of the shell only reaching about 5 m/s^2 instead of 9.8 m/s^2. Despite the errors in the force reconstruction, dividing the force vector magnitude by the acceleration vector magnitude yields a mean mass of 50.4 grams. Thus, moving through a variety of orientations, on average the robot is able to successfully measure the load on its shell. Additionally, the reconstructed accelerations follow the accelerometer traces reasonably well, with a mean error angle between the two vectors of 18.8 degrees. Therefore without an accelerometer, the robot would still be able to determine the approximate direction of the gravity vector acting on it using data from the shell alone.
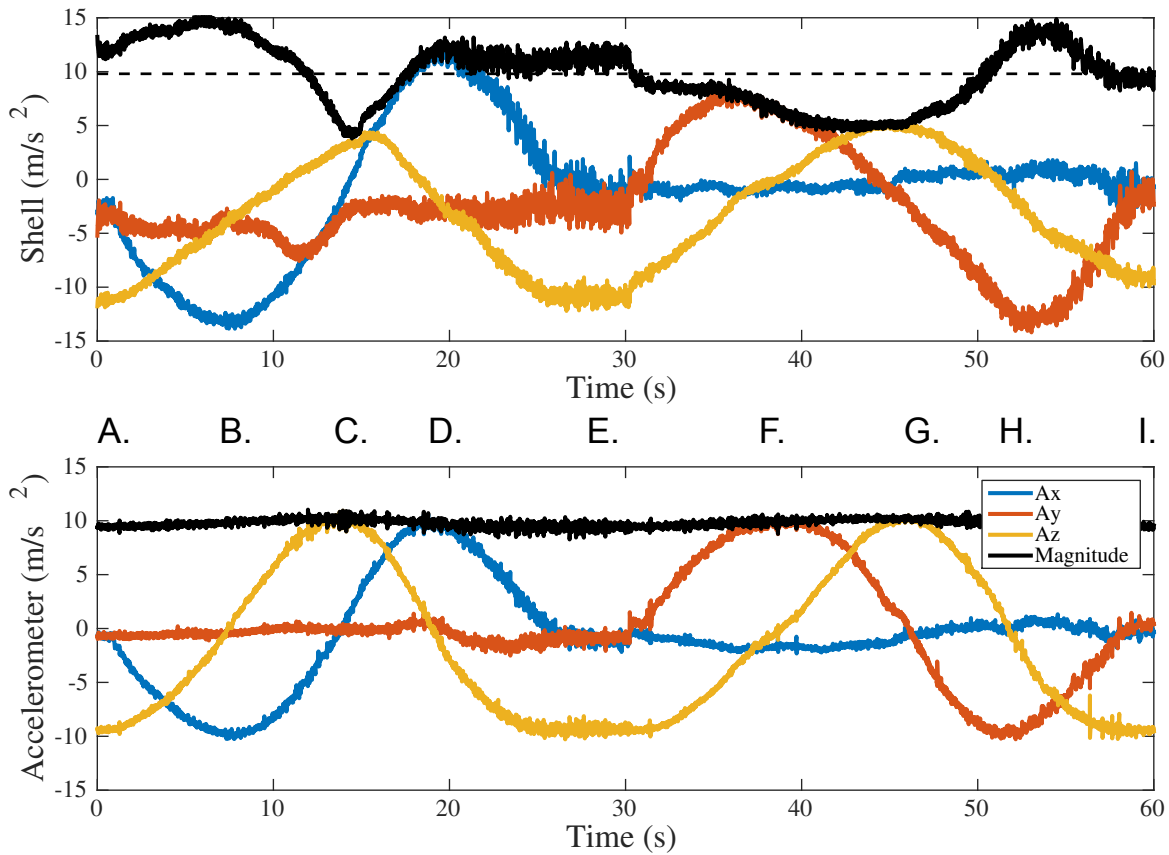
Figure 3.3: A comparison of the acceleration traces measured by both the shell and the accelerometer on board the VelociRoACH. The robot is slowly rotated first clockwise around its *y*-axis and then clockwise around its *x*-axis. Each letter marks a different orientation of the robot in the rotation sequence: A. legs down; B. nose up; C. legs up; D. nose down; E. legs down; F. left side down; G. legs up; H. left side up; I. legs down.

Step Response

A step response experiment was used to determine how quickly the sensor would respond to weight being added to the robot, as well as the accuracy of the measurement. In Fig. 3.5a, the VelociRoACH can be seen inverted with 50 grams resting on its underside. The mass was dropped onto the robot from a height of about 0.5 cm, and lifted off four seconds later. The reconstructed forces as well as *z*-axis accelerometer data are plotted in Fig. 3.5b. Ringing is apparent at approximately 15 Hz, resulting from the spring-mass-damper system. This frequency is less than the leg frequency that the robot can operate at, so the springs and reflector system will be excited at its resonant frequency by the motion
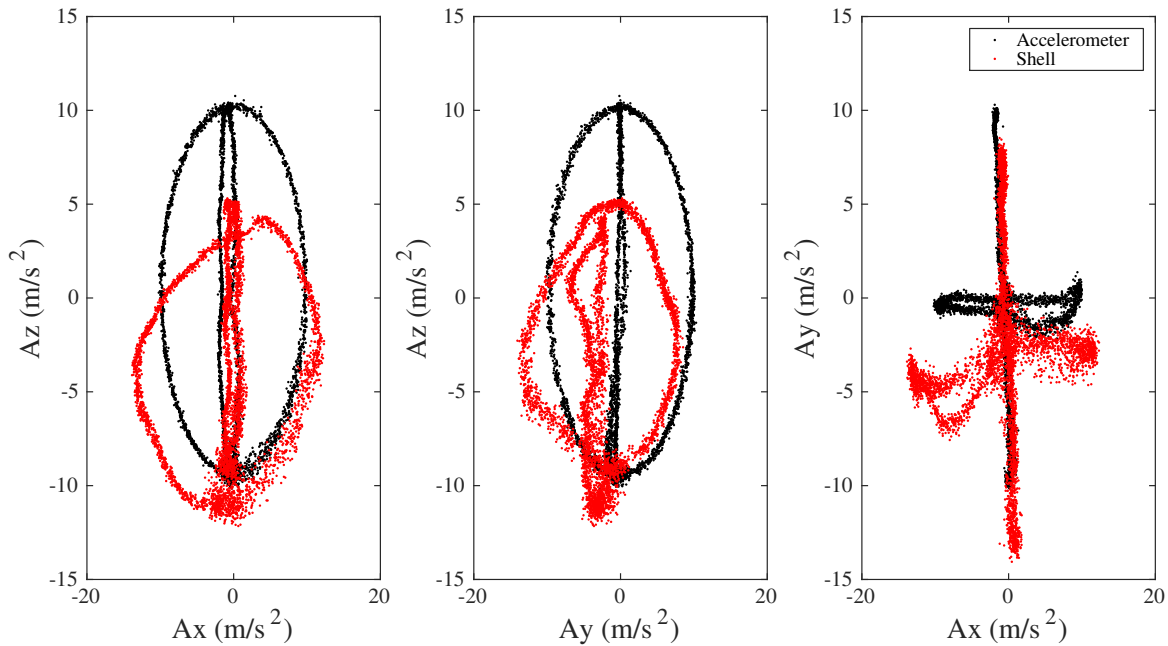
Figure 3.4: Slices of the three-dimensional acceleration vector space for the data from both the accelerometer and the shell through the rotation sequence of the robot.

of the robot. In future work, damping will be added to reduce shell ringing.

The z-axis accelerometer data demonstrates that an impact occurred at $t = 1$ second, however it is unclear from this data whether or not the object remained on the robot. Upon inspecting the reconstructed F_z data, it is apparent that for the period from 1-4 seconds, there is a force of about -0.5 N on the robot, which is approximately the force of a 50 gram mass. Using this method, the sensor fit was validated for masses up to 150 grams placed on the robot in the z-axis, and up to 70 grams in the x- and y-axes.

Collision Detection

To demonstrate operation of the force-torque sensor during locomotion with contact, the robot was run into obstacles as shown in Fig. 3.6a. The corresponding forces, leg torques, and integrated z-axis gyroscope data for the VelociRoACH are in Fig. 3.6b. This experiment had multiple stages. For section [I], in which the robot is at rest, the measured forces are nominally static and zero, as expected. Once the robot starts walking with a stride frequency of 2 Hz, as indicated in the leg torque data, the force data begins to os-
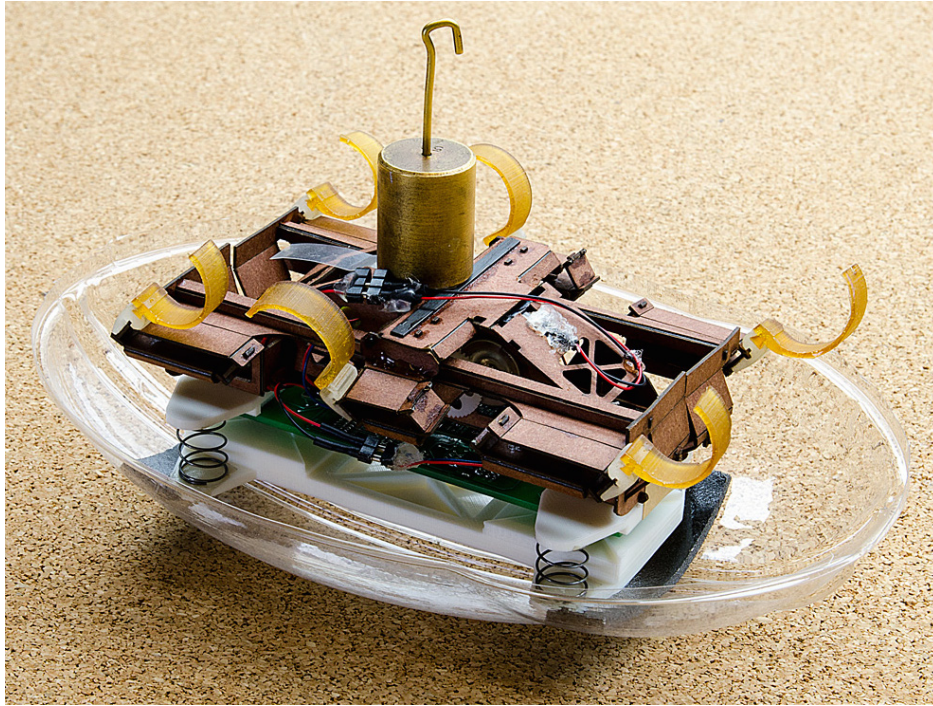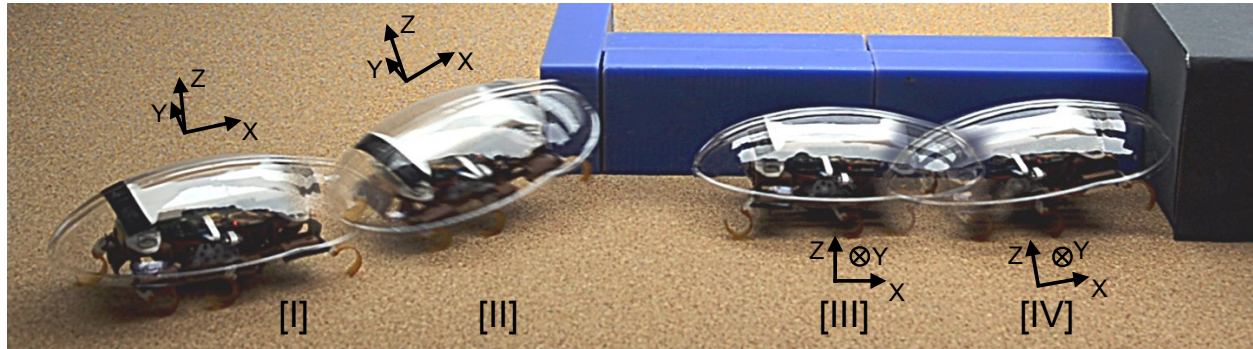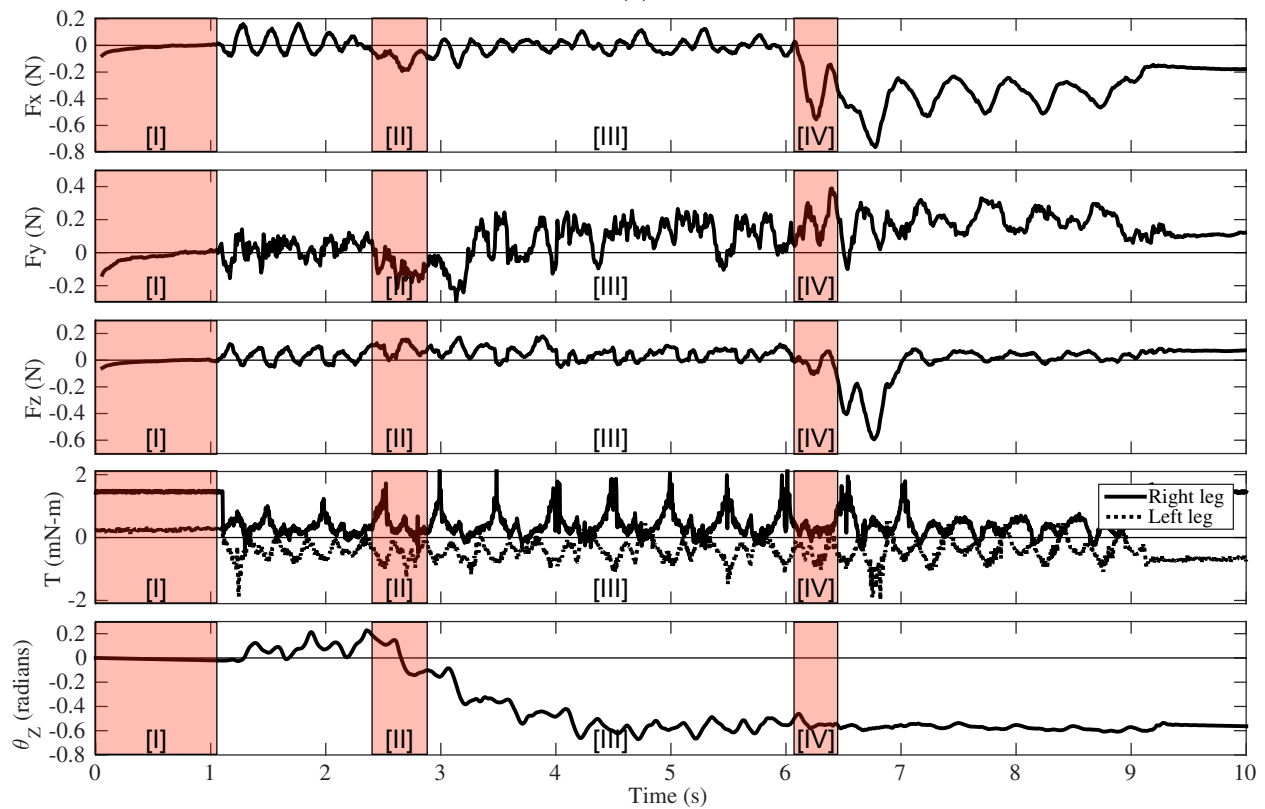
(a)
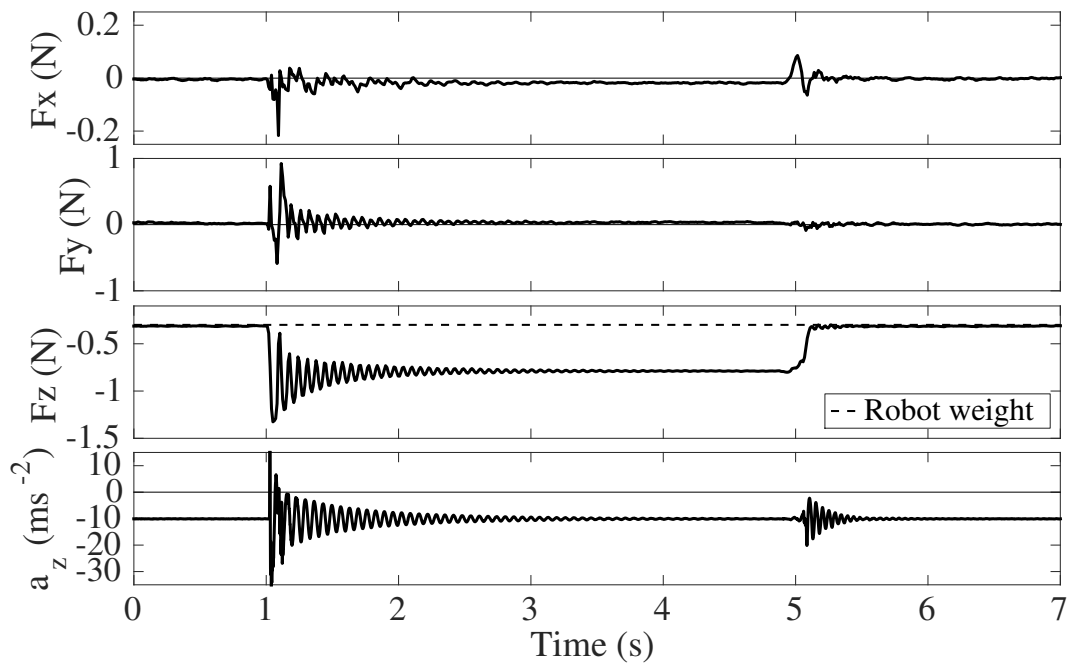
(b)

Figure 3.5: Step response of sensor to a 50 gram mass. (a) Photo of VelociRoACH on its back with a 50 gram mass resting on its underside. (b) Three-axis force data and *z*-axis accelerometer data for a 50 gram mass placed on the robot at 1 second and removed at 5 seconds.

Figure 3.6: The VelociRoACH in (a) is shown stationary [I], running into a corner [II], following a wall [III], and colliding with a perpendicular wall [IV]. The corresponding x, y, and z forces, as well as the right and left leg torques and the integrated z-axis gyroscope data are shown in (b).

cillate due to this motion, bounded by ± 0.15 N. In section [II] when the robot collides with the corner, there is a negative spike in F_x and F_y of approximately -0.2 N. The signs of these forces are expected, because the collision occurs on the front-left corner of the shell, causing the robot to turn to the right. This is also substantiated by the θ_z gyroscope data in section [II] of Fig. 3.6b. In section [III], a negative F_y was expected as a result of the robot repeatedly contacting the wall on its left side. However, the sensor forces and torques indicate the possibility of complex dynamic contacts during this interval which merit further study. In section [IV], the sensor measures a sharp spike of -0.5 N for F_x, a result of the perpendicular collision between the robot and the wall. The sign and magnitude of this force are as expected, since the shell is displaced along the negative x-axis in the collision, and the magnitude is equal to the maximum thrust force the 0.7 N robot can produce, approximately 0.5 N. This was calculated using the coefficient of static friction of the robot on corkboard, $\mu_s = 0.7$, which varies with leg position. For the following 2 seconds as the robot continues to collide with the wall, the F_x data oscillates with a period of 2 Hz (the stride frequency) between -0.2 N and -0.5 N, which identifies and measures the repeated collision. The force data corresponding to the complicated motion and contact conditions in Fig. 3.6 demonstrates the utility of the sensor, and the potential for the VelociRoACH to not only detect collisions, but also characterize the contact forces involved.

Chapter 4

Conclusions

A planar sensor was developed using photointerrupters and a reflector surface which partially decouples motions in order to measure the forces and torques applied to the shell of a millirobot. This sensor will enable the robot to better interact with its environment by providing intelligence about the objects it encounters with good sensitivity, as seen in Table 4.1, which compares the sensing ranges and resolutions of the SkinProc to those of a commercial sensor. In future work, the calibration method can be improved in order to reduce force estimation error, so that the contact location of the force on the shell can be calculated. Also, new shell designs can be explored that encompass the entire robot body, in order to detect high-centering or to measure the drag force from the ground when in motion.

Table 4.1: Range and resolution of force-torque sensors. Each cell of the table is displayed as range/resolution.
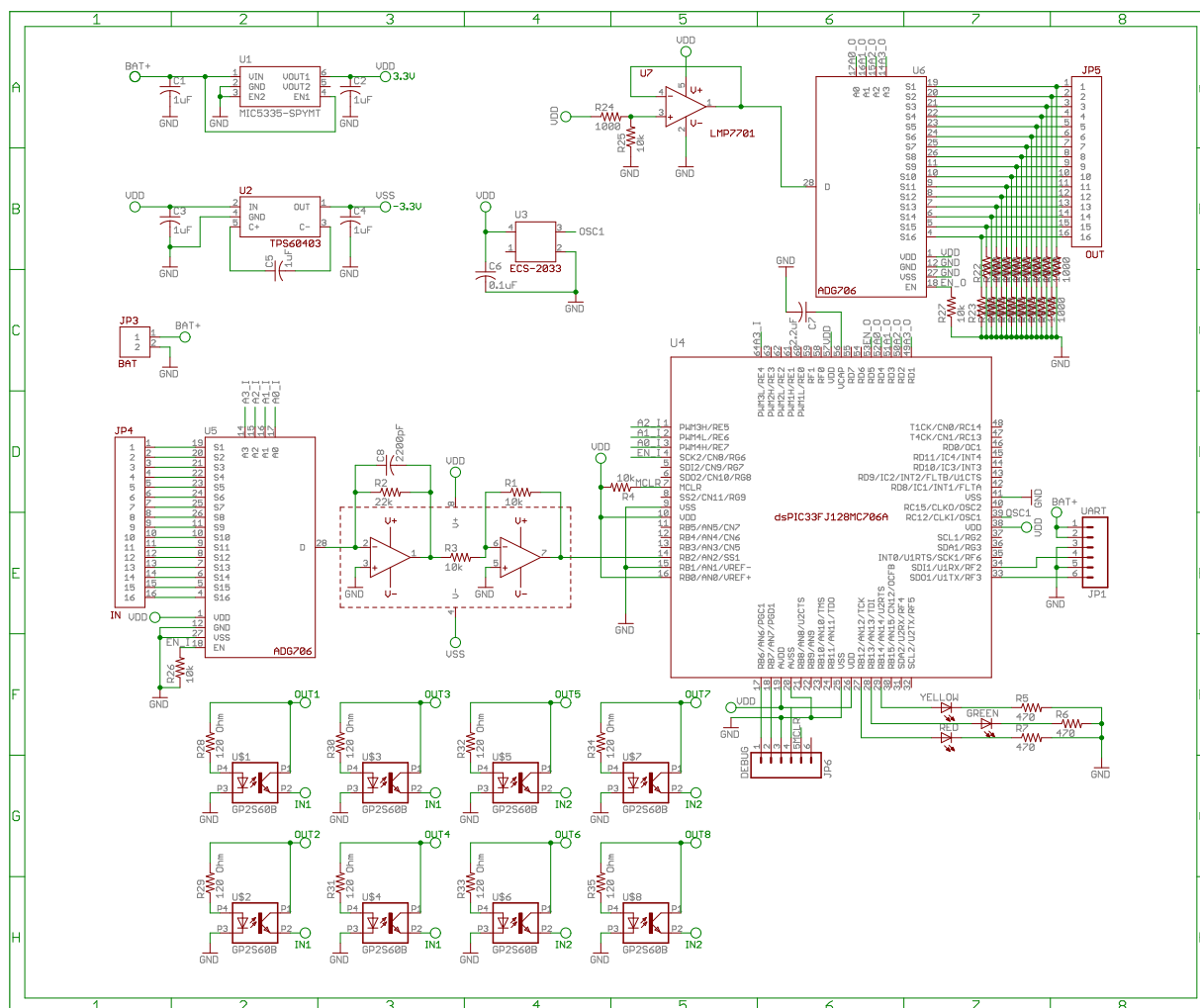
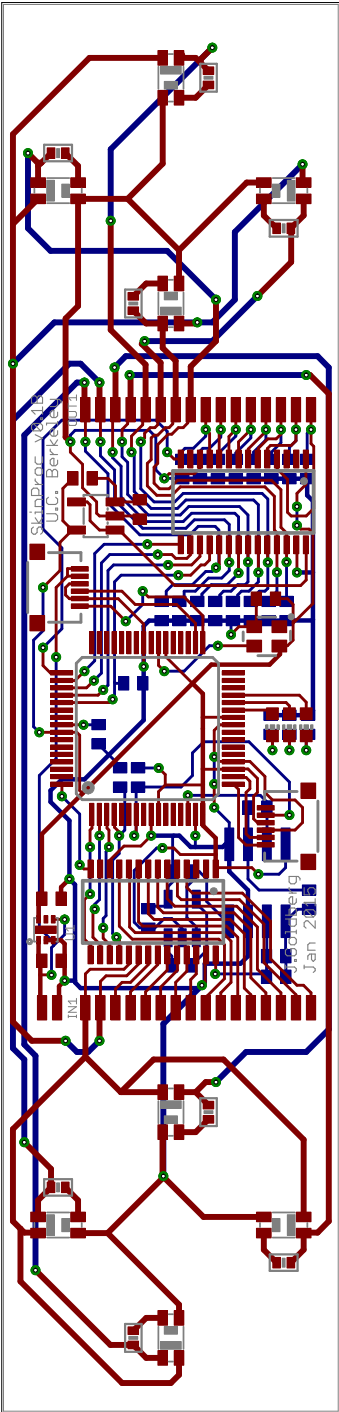|	F_x (N)	F_y (N)	F_z (N)	M_x (mN-m)	M_y (mN-m)	M_z (mN-m)
SkinProc	2.3/.0054	2.1/.0167	1.9/.0051	96/0.72	127/0.25	138/0.44
ATI Nano43	18/.0039	18/.0039	18/.0039	250/0.05	250/0.05	250/0.05

Acknowledgments

Appendix A

SkinProc Schematic

Appendix B

SkinProc Layout

Bibliography

[1] R. Bajcsy. "Active perception". In: *Proceedings of the IEEE* 76.8 (1988), pp. 966–1005. ISSN: 0018-9219. DOI: `10.1109/5.5968`.

[2] A. Bicchi. "Intrinsic contact sensing for soft fingers". In: *IEEE Int. Conf. on Robotics and Automation*. 1990, 968–973 vol.2. DOI: `10.1109/ROBOT.1990.126117`.

[3] Antonio Bicchi, J Kenneth Salisbury, and David L Brock. "Contact sensing from force measurements". In: *The International Journal of Robotics Research* 12.3 (1993), pp. 249–262.

[4] J. Borenstein and Y. Koren. "Obstacle avoidance with ultrasonic sensors". In: *Robotics and Automation, IEEE Journal of* 4.2 (1988), pp. 213–218. ISSN: 0882-4967. DOI: `10.1109/56.2085`.

[5] Duncan W Haldane et al. "Integrated Manufacture of Exoskeleton and Sensing for Folded Millirobots". In: *Journal of Mechanisms and Robotics* 7(2) (2015).

[6] D.W. Haldane, K.C. Peterson, F.L. Garcia Bermudez, and R.S. Fearing. "Animal-inspired design and aerodynamic stabilization of a hexapedal millirobot". In: *IEEE Int. Conf. on Robotics and Automation*. 2013, pp. 3279–3286. DOI: `10.1109/ICRA.2013.6631034`.

[7] S. Hirose and K. Yoneda. "Development of optical six-axial force sensor and its signal calibration considering nonlinear interference". In: *IEEE Int. Conf. on Robotics and Automation*. 1990, 46–53 vol.1. DOI: `10.1109/ROBOT.1990.125944`.

[8]   A.M. Hoover and R.S. Fearing. "Fast scale prototyping for folded millirobots". In: *IEEE Int. Conf. on Robotics and Automation*. 2008, pp. 886–892. DOI: `10.1109/ROBOT.2008.4543317`.

[9]   Jaakko Karras. "Tactile Sensors for Palm-Size Crawling Robots". MA thesis. EECS Department, University of California, Berkeley, 2014. URL: `http://www.eecs.berkeley.edu/Pubs/TechRpts/2014/EECS-2014-40.html`.

[10]   J.T. Karras, D.W. Haldane, and R.S. Fearing. "Rapid-manufacturable hair sensor array for legged millirobots". In: *IEEE/RSJ Int. Conf. on Intelligent Robots and Systems*. 2012, pp. 1956–1962. DOI: `10.1109/IROS.2012.6386143`.

[11]   A.G. Lamperski, O.Y. Loh, B.L. Kutscher, and N.J. Cowan. "Dynamical Wall Following for a Wheeled Robot Using a Passive Tactile Sensor". In: *IEEE Int. Conf. on Robotics and Automation*. 2005, pp. 3838 –3843. DOI: `10.1109/ROBOT.2005.1570706`.

[12]   J. Lee, S.N. Sponberg, O.Y. Loh, A.G. Lamperski, R.J. Full, and N.J. Cowan. "Templates and Anchors for Antenna-Based Wall Following in Cockroaches and Robots". In: *Robotics, IEEE Transactions on* 24.1 (2008), pp. 130 –143. ISSN: 1552-3098. DOI: `10.1109/TRO.2007.913981`.

[13]   P. Liljeback, K.Y. Pettersen, and O. Stavdahl. "A snake robot with a contact force measurement system for obstacle-aided locomotion". In: *IEEE Int. Conf. on Robotics and Automation*. 2010, pp. 683–690. DOI: `10.1109/ROBOT.2010.5509839`.

[14]   P. Liljeback, O. Stavdahl, K.Y. Pettersen, and J.T. Gravdahl. "A modular and waterproof snake robot joint mechanism with a novel force/torque sensor". In: *IEEE/RSJ Int. Conf. on Intelligent Robots and Systems (IROS)*. 2012, pp. 4898–4905. DOI: `10.1109/IROS.2012.6386115`.

[15]   R.A. Russell and J.A. Wijaya. "Object location and recognition using whisker sensors". In: *Australasian Conf. on Robotics and Automation*. 2003.

[16]   K. Sabe, M. Fukuchi, J.-S. Gutmann, T. Ohashi, K. Kawamoto, and T. Yoshigahara. "Obstacle avoidance and path planning for humanoid robots using stereo vision".

In: *IEEE Int. Conf. on Robotics and Automation*. Vol. 1. 2004, 592–597 Vol.1. DOI: `10.1109/ROBOT.2004.1307213`.

[17] F.W. Sinden and R.A. Boie. "A planar capacitive force sensor with six degrees of freedom". In: *IEEE Int. Conf. on Robotics and Automation*. Vol. 3. 1986, pp. 1806–1814. DOI: `10.1109/ROBOT.1986.1087452`.

[18] T. Tsuji, Y. Kaneko, and S. Abe. "Whole-Body Force Sensation by Force Sensor With Shell-Shaped End-Effector". In: *Industrial Electronics, IEEE Transactions on* 56.5 (2009), pp. 1375–1382. ISSN: 0278-0046. DOI: `10.1109/TIE.2009.2014748`.

[19] Richard M Voyles, J Daniel Morrow, and Pradeep K Khosla. "The shape from motion approach to rapid and precise force/torque sensor calibration". In: *Journal of dynamic systems, measurement, and control* 119.2 (1997), pp. 229–235.

[20] J.A. Wijaya and R.A. Russell. "Object exploration using whisker sensors". In: *Australasian Conf. on Robotics and Automation*. 2002, pp. 180–185.